



Cite this: *Nanoscale*, 2017, 9, 17788

Fast-switching electrochromic properties of mesoporous WO₃ films with oxygen vacancy defects†

Bon-Ryul Koo ^a and Hyo-Jin Ahn ^{*a,b}

In this study, mesoporous WO₃ films with oxygen vacancy defects have been fabricated using the camphene-assisted sol-gel method. By controlling the optimized weight ratio of camphene on the WO₃ films, we developed a unique film structure of the WO₃ phase with both mesoporous morphology and oxygen vacancy defects due to the distinctive effect of camphene. The mesoporous WO₃ films with oxygen vacancy defects fabricated using 10 wt% camphene showed superb multifunctional electrochromic (EC) properties with both fast switching speeds (5.8 s for coloration speed and 1.0 s for bleaching speed) and high coloration efficiency (CE, 51.4 cm² C⁻¹), which include the most prominent properties, particularly for switching speeds among WO₃-based films reported so far. The attractive EC properties are due to the synergistic effects of the mesoporous morphology and oxygen vacancy defects on the WO₃. The fast switching speeds are mainly caused by the reduced Li⁺ diffusion pathway due to the mesoporous morphology and increased electrical conductivity due to the oxygen vacancy defects. In addition, the increased CE value is due to the large transmittance modulation as a result of a more effective electrostatic contact of the mesoporous morphology and an increased optical bandgap of the oxygen vacancy defects on the WO₃. Therefore, this unique film structure of the mesoporous WO₃ films with oxygen vacancy defects can be potentially regarded as a novel EC material for high-performance EC devices.

Received 12th September 2017,
Accepted 17th October 2017

DOI: 10.1039/c7nr06796h

rsc.li/nanoscale

Introduction

Due to low power consumption, stable memory effect, and high coloration efficiency (CE), electrochromic (EC) devices that are capable of reversibly converting their optical properties (transmittance, reflection, and absorption) in a small electric field are considered to be highly promising candidates for prospective applications, such as digital displays, smart windows, and rear view mirrors, among many others.^{1–3} Typically, EC devices are assembled with four functionalized layers: two different EC layers, the ion conductor layer, and the transparent conducting layer.⁴ EC layers are a particularly important component that dominates the EC properties, which is attributed to the intercalation/deintercalation of ions (H⁺ and Li⁺) into/out of the host lattice of EC films. They can be divided into two types: cathodic (WO₃, MoO₃, polythio-

phene derivatives, *etc.*) and anodic (NiO, IrO₂, polyaniline, *etc.*) EC materials.⁵

Among various EC materials, WO₃, which is an indirect semiconductor with a band gap of 2.5–3.65 eV, has received extensive attention as a representative cathodic EC material due to its distinctive advantages of harmlessness, low cost, and stability in acidic and oxidative environments, making it useful for EC devices.^{6,7} The WO₃ can convert the optical properties from transparent to a deep blue colour based on the reversible electrochemical double behaviour of ions and electrons.⁷ In general, it is well-known that the EC properties of the WO₃, including the switching speed and CE, depend on the interface reaction process with an electrolyte and the ion diffusion process, which are mainly determined by the morphology, crystallinity, and the electronic structure of the formed WO₃ films.^{8,9} Therefore, much previous research to fabricate the WO₃ films for EC devices has been conducted using the sol-gel method, anodic growth method, spray pyrolysis, sputtering method, electrochemical deposition method, and chemical vapor deposition method.^{10–15}

Owing to the rapid commercialization of EC devices, numerous efforts have been devoted to obtaining superb EC properties of the WO₃ films, such as transmittance modulation, CE, and switching speed. In particular, a porous struc-

^aProgram of Materials Science & Engineering, Convergence Institute of Biomedical Engineering and Biomaterials, Seoul National University of Science and Technology, Seoul 01811, Korea

^bDepartment of Materials Science and Engineering, Seoul National University of Science and Technology, Seoul 01811, Korea. E-mail: hjahn@seoultech.ac.kr

†Electronic supplementary information (ESI) available. See DOI: 10.1039/c7nr06796h

ture is generally expected to provide more effective electroactive sites with the electrolyte and to reduce the diffusion length of ions within the WO_3 due to their high specific surface area, enhancing their switching speed or CE.^{10,15} For example, Yang *et al.* reported the preparation of porous WO_3 films using the templated-assisted sol-gel method, which exhibited a high CE ($50.1 \text{ cm}^2 \text{ C}^{-1}$) and fast switching speeds (5.1 s for coloration speed and 8.7 s for bleaching speed).¹⁰ Furthermore, Li *et al.* synthesized mesoporous WO_3 films through the hot-wire chemical vapour deposition method by adjusting the filament temperature, substrate temperature, and oxygen partial pressure.¹⁵ These films have a higher CE value ($38.0 \text{ cm}^2 \text{ C}^{-1}$) than that of the dense WO_3 films ($20.0 \text{ cm}^2 \text{ C}^{-1}$).¹⁵ However, the experimental process for fabricating the porous WO_3 films proposed by Cai *et al.* and Li *et al.* suffers from the complex multi-step fabrication procedure, which can limit its commercialization. Moreover, forming oxygen vacancy defects on the WO_3 could be an innovative strategy to improve the switching speed due to the reduced charge transfer resistance.^{14,16} Bathe *et al.* reported that, while the WO_3 films with oxygen vacancies prepared by the spray pyrolysis method exhibit a good CE ($42.0 \text{ cm}^2 \text{ C}^{-1}$), their transmittance modulation (25.0%) is still low when compared to WO_3 films.¹⁶ However, none of the previous studies has attempted to simultaneously apply the mesoporous morphology and oxygen vacancy defects on the WO_3 -based films.

In this study, we constructed mesoporous WO_3 films with oxygen vacancy defects as a novel film structure using the camphene-assisted sol-gel method. The sol-gel technique is a common method of film production that allows for a large-area deposition at a low cost and provides simple control of the film structure.¹⁷ Camphene plays a particularly attractive role of simultaneously a mesopore-forming agent and a source forming oxygen vacancy defects, leading to the formation of unique WO_3 films with both fast switching speeds and high CE. In addition, we demonstrated the effect of camphene as an organic additive on their structural, chemical, morphological, electrochemical, and EC properties, as well as the mechanism for improving their EC properties.

Results and discussion

We fabricated mesoporous WO_3 films with oxygen vacancy defects through the camphene-assisted sol-gel method. To investigate the formation mechanism of the mesoporous morphology on the films using camphene, the measurement of TGA on the precursor solutions with varied weight ratios of camphene was performed at temperatures in the range of 25 to 300 °C in air (see Fig. 1a). All samples displayed a rapid weight loss of ca. 80.0 wt% at 25–70 °C, corresponding to the evaporation of the solvent. Then, the critical variation of the weight loss among the samples was found at 70–110 °C, as shown in the detailed TGA curves (see Fig. 1b). For the precursor solution without camphene (bare WO_3), the weight loss was continuously generated up to 120 °C due to the hydrolysis of WCl_6

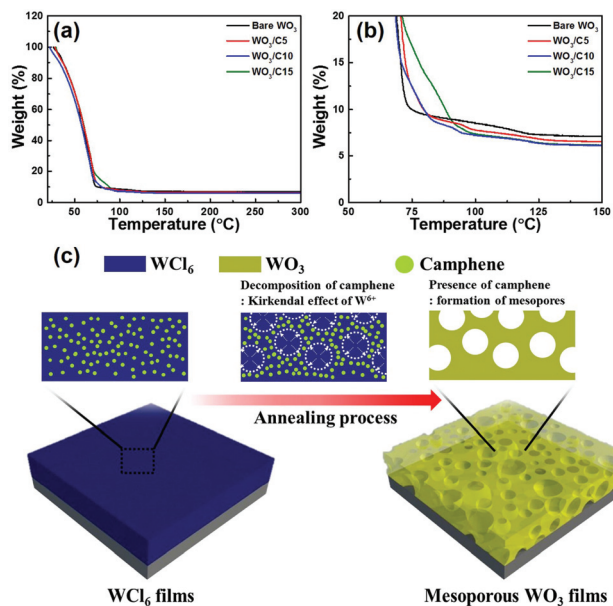


Fig. 1 (a) TGA curves of bare WO_3 , $\text{WO}_3/\text{C5}$, $\text{WO}_3/\text{C10}$, and $\text{WO}_3/\text{C15}$ from 25 to 300 °C in air, (b) detailed TGA curves of the samples in the range of 70–110 °C, and (c) a schematic of the formation mechanism for the mesoporous WO_3 films prepared by the camphene-assisted sol-gel method.

for forming the WO_3 .¹⁸ On the other hand, the precursor solutions with camphene presented an additional weight loss of 0.71% for $\text{WO}_3/\text{C5}$, 1.28% for $\text{WO}_3/\text{C10}$, and 1.15% for $\text{WO}_3/\text{C15}$, as compared to bare WO_3 at 100 °C. This is caused by the thermal decomposition of camphene in the precursor solutions, which can simultaneously accelerate the diffusion of W^{6+} outside the samples.¹⁹ However, despite the high weight ratio of camphene, $\text{WO}_3/\text{C15}$ shows a weight loss similar to that of $\text{WO}_3/\text{C10}$, which indicates the presence of residual carbon because of excessive camphene, causing the dense morphology of the films. Based on the TGA results, we can suggest the formation mechanism of the mesoporous morphology using camphene. As shown in Fig. 1c, camphene can lead to the formation of isobornyl alkyl ether with W^{6+} . That is, as hydrophobic camphene can be converted to hydrophilic isobornyl alkyl ether by 2-propanol with alcohol, camphene can interact with W^{6+} electrostatically.^{19,20} Therefore, due to a higher diffusion coefficient of camphene ($D = 12 \times 10^{-8} \text{ m}^2 \text{ s}^{-1}$) as compared to that of pure W^{6+} ($D = 70 \times 10^{-8} \text{ m}^2 \text{ s}^{-1}$), the thermal decomposition of camphene during annealing can lead to the acceleration of the Kirkendal effect of W^{6+} that interacted with isobornyl alkyl ether, which is proved as Fick's first law (see eqn (1)):^{21,22}

$$J = -D(\text{d}C/\text{d}x) \quad (1)$$

where J is the flux, D is the diffusion coefficient, and $\text{d}C/\text{d}x$ is the concentration gradient. As a result, the presence of camphene can generate mesopores due to the Kirkendal effect of

W^{6+} , resulting in the formation of the mesoporous morphology on the EC films.

To investigate the effect of camphene on the morphology, Fig. 2 displays (a–d) top-view and (e–h) cross-view FESEM images of bare WO_3 , $WO_3/C5$, $WO_3/C10$, and $WO_3/C15$, respectively. In general, the pure FTO glass has a morphology where crystallites are sequentially interlocked over the surface.²³ After coating the precursor solutions, the film structures with a smooth morphology (168.0–196.0 nm in thickness) were formed on the FTO glass by solvent evaporation during spin-coating. This result is equally presented in the FESEM results obtained from bare WO_3 (see Fig. S1a†) and $WO_3/C10$ (see Fig. S1b†) before the annealing. After the annealing (Fig. 2a–d), it can be observed that all samples consist of ultrafine nanoparticles with a diameter of 7.9–11.8 nm throughout the crystallite surface of the FTO glass due to the WO_3 formed by the hydrolysis of WCl_6 .²⁴ Interestingly, the gradual variation of the morphologies among the samples is observed with an increase of the weight ratios of camphene. As shown in Fig. 2a, bare WO_3 reveals a dense morphology. On the other hand, $WO_3/C5$ and $WO_3/C10$ show a rough morphology with mesopores (14.4–25.2 nm for $WO_3/C5$ and 22.6–34.1 nm for $WO_3/C10$), in which, with an increase of the weight ratios of camphene, the size and distribution of the mesopores gradually increase from $WO_3/C5$ (Fig. 2b) to $WO_3/C10$ (Fig. 2c). This indicates that the increase of the weight ratio of camphene can lead to the formation of a large number of mesopores due to the Kirkendal effect by the decomposition of camphene during the annealing process. However, due to the presence of residual carbon from excessive camphene confirmed by the TGA result (Fig. 1b), $WO_3/C15$ (Fig. 2d) exhibits a smooth morphology. In the cross-view FESEM images (Fig. 2e–h), their thicknesses are observed to be 164.0–192.0 nm for bare WO_3 , 160.2–196.1 nm for $WO_3/C5$, 160.2–192.0 nm for $WO_3/C10$, and 160.0–188.0 nm for $WO_3/C15$, meaning that the different weight ratios of camphene do not affect the thickness of the samples. Therefore, the SEM results show that $WO_3/C10$ has a higher mesoporous morphology as compared to other samples, which is useful to the Li^+ intercalation/deintercalation capacity and the ion diffusion

in terms of improving the transmittance modulation and switching speed, respectively, in the EC properties.¹⁰

To characterize the chemical binding states of all samples, XPS measurements were conducted. All binding energies were standardized with the C 1s of 284.5 eV as a reference. From the W 4f XPS core-level spectra (Fig. 3a), two pairs of doublets for W 4f_{7/2} and W 4f_{5/2} photoelectrons were observed; the lower-energy peaks at 34.2 eV correspond to the binding energy of W^{5+} and the higher-energy peaks at 35.2 eV indicate that of W^{6+} .^{25,26} Obviously, with an increase of the weight ratio of camphene, the area ratios of W^{5+}/W^{6+} peaks gradually increased from 16.6% for $WO_3/C5$ to 22.1% for $WO_3/C15$ due to the emergence of an oxygen vacancy defect state between the conduction and valence bands,^{27,28} which is proved by the reduced peak area of W–O in the O 1s XPS core-level spectra (see Fig. 3b). In addition, to further confirm the presence of oxygen vacancy defects of the WO_3 due to camphene, we calculated the atomic ratio of O/W using the W 4f and O 1s XPS core-level spectra (see Fig. 3c). The calculated atomic ratio of O/W is 3.06 for bare WO_3 , 2.94 for $WO_3/C5$, 2.89 for $WO_3/C10$, and 2.79 for $WO_3/C15$. These results suggest that an increase of the weight ratio of camphene leads to an increased number of oxygen vacancy defects.²⁷ In general, the carbon used as a reducing agent takes the oxygen from the metal oxide by a carbothermic reaction forming CO_2 or CO , as indicated by L'vov *et al.*²⁹ Therefore, the thermal decomposition of camphene generated at 100 °C can cause the formation of WO_3 with oxygen vacancy defects by partial reduction of WO_3 , thus affecting their electrical and optical properties relative to the EC properties. In addition, the XRD results (see Fig. S2†) of all samples reveal broad diffraction peaks at *ca.* 23.1°, indicating the amorphous structure of the formed films. This is useful to the EC properties owing to their loose structure to facilitate fast ion diffusion.^{30,31}

In order to identify Li^+ intercalation/deintercalation of the samples during the electrochromic reaction, CV measurement

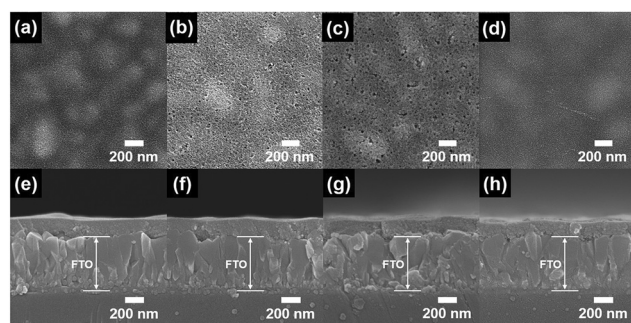


Fig. 2 (a–d) Top-view and (e–h) cross-view FESEM images of bare WO_3 , $WO_3/C5$, $WO_3/C10$, and $WO_3/C15$, respectively.

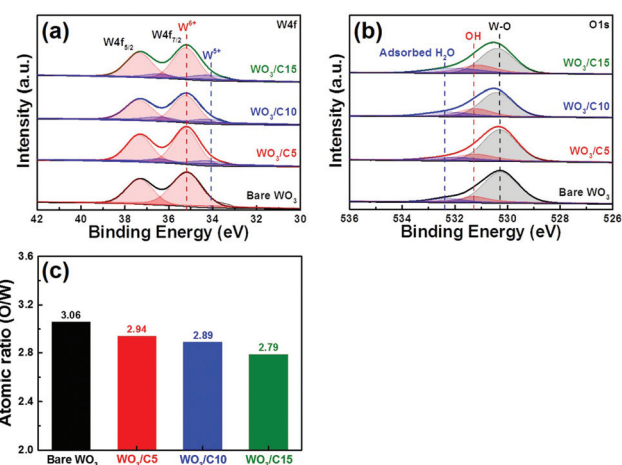


Fig. 3 (a) W 4f and (b) O 1s XPS core-level spectra obtained from bare WO_3 , $WO_3/C5$, $WO_3/C10$, and $WO_3/C15$, and (c) the atomic ratio of O/W obtained from the samples.

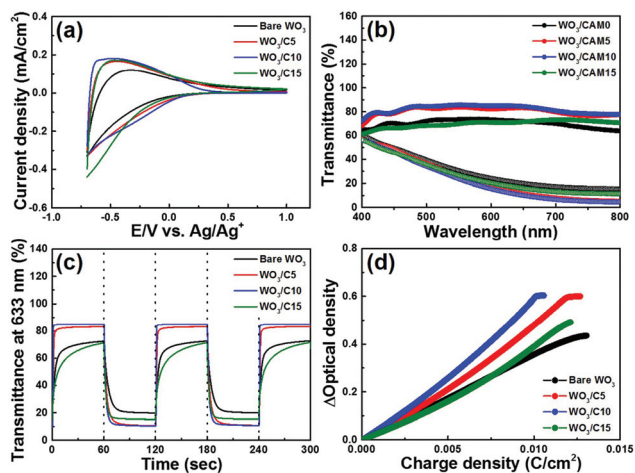
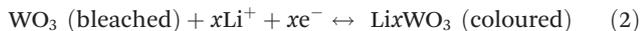


Fig. 4 (a) CV curves of the samples in a 1 M LiClO₄-PC electrolyte at a scan rate of 20 mV s⁻¹ in the potential range of -0.7 to 1.0 V with a three-electrode system. (b) Transmittance spectra applied at -0.7 V for the coloured state (dotted line) and 1.0 V for the bleached state (solid line) between 400 and 800 nm, (c) *in situ* optical responses for 60 s per step measured at 633 nm, and (d) variation of the optical density with respect to the charge density.

was performed. Fig. 4a shows the CV curves measured in a 1 M LiClO₄ electrolyte in the potential region of -0.7 to 1.0 V (*vs.* Ag wire) at a scan rate of 20 mV s⁻¹. During the CV profiling, the reversible colour change of the samples from deep blue (coloured state) to transparent (bleached state) is caused by the accompanying intercalation/deintercalation of Li⁺ into/out of the samples (see Fig. S3†), which could be explained by using the following equation (see eqn (2)):⁹



In addition, we found that both the anodic and cathodic current density increased with an increase of the weight ratio of camphene. This indicates an increase of electrochemical activity due to their mesoporous morphology, providing a more effective electrostatic contact between the electrode and the electrolyte.^{9,14} However, for WO₃/C10, while the cathodic current density is higher than the others due to the increased electrical conductivity by the oxygen vacancy defects, there is a decrease in the anodic current density because of their dense morphology by the residual carbon. Overall, this indicates that WO₃/C10 has the highest electrochemical activity relative to the superior electrochromic properties when compared to other samples;¹⁴ these are summarized in Table 1. To quantitatively compare the electrochromic properties of the samples,

the UV-vis transmittance curve was measured under an applied potential of -0.7 (coloured state) and 1.0 V (bleached state). As shown in Fig. 4b, the transmittance modulation ($\Delta T = T_b - T_c$, where T_b and T_c are transmittance in bleached and coloured states, respectively) gradually increased from bare WO₃ (51.2% at 633 nm) to WO₃/C10 (73.3% at 633 nm), resulting from the decreased transmittance in the coloured state by the increased Li⁺ intercalation capacity due to the mesoporous morphology and the increased transmittance in the bleached state due to the increase of the optical bandgap (see Fig. S4a†). In particular, increasing camphene in the WO₃ can cause an increase of the electron concentration induced by the oxygen vacancy defects, resulting in an increase of both the optical bandgap (see Fig. S4a†),³²⁻³⁴ by lifting the Fermi level into the conduction band, and the electrical conductivity (see Fig. S4b†).^{35,36} On the other hand, for WO₃/C15, there is a decreased transmittance modulation, which is due to the presence of the residual carbon. Therefore, it can be seen that the transmittance modulation of WO₃/C10 is much larger than the other samples. In order to characterize the switching speeds of the samples, the investigation of the *in situ* optical response to be modulated at 633 nm under the potential range between -0.7 and 1.0 V (see Fig. 4c) was carried out using chronoamperometry. The switching speeds were calculated as the time required to achieve 90% of the entire transmittance modulation at 633 nm. Interestingly, the switching speeds were improved from bare WO₃ (11.8 s for coloration speed and 14.6 s for bleaching speed) to WO₃/C10 (5.8 s for coloration speed and 1.0 s for bleaching speed), which is due to the synergistic effect of the mesoporous morphology that reduces the Li⁺ diffusion pathway and WO₃ with increased oxygen vacancy defects that enhances the electrical conductivity, facilitating Li⁺ and electron diffusion intercalation/deintercalation processes.³⁷ For WO₃/C15, while there was a maximum coloration speed of 5.6 s due to the increased electrical conductivity, the bleaching speed rapidly degraded to 28.8 s as a result of the dense morphology formed by the residual carbon, which has difficulty in causing Li⁺ deintercalation out of the WO₃. Therefore, the switching speeds of WO₃/C10 in this study demonstrate the highest performance, as compared to those of many WO₃-based materials reported in previous research (see Table S1†).^{2,9,10,15,38-45} More interestingly, WO₃/C10 sustains a transmittance modulation of 81.6% of its initial value after 1000 cycles while bare WO₃ has a degraded transmittance modulation after 1000 cycles (61.7% of its initial value), as shown in Fig. S5† This result can be attributed to the mesoporous morphology of WO₃/C10 with oxygen vacancy defects to facilitate the intercalation/deintercalation of Li⁺ and decrease

Table 1 Summary of the electrochromic properties obtained from all the samples

Samples	T_b (%)	T_c (%)	Transmittance modulation (%)	Coloration speed (s)	Bleaching speed (s)	CE (cm ² C ⁻¹)
Bare WO ₃	72.4	21.2	51.2	11.8	14.6	34.5
WO ₃ /C5	83.1	13.2	69.9	8.0	2.3	42.2
WO ₃ /C10	84.9	11.6	73.3	5.8	1.0	51.4
WO ₃ /C15	70.9	17.2	53.7	5.6	28.8	32.1

the trapping of ions during cycling, thus resulting in good cycling stability of the films.^{39,41,42} In addition, the CE corresponding to the most important criteria is used to determine the EC properties, which is represented as the change in the optical density (OD) per unit charge density (Q/A) during the switching and can be calculated using the following equations (see eqn (3) and (4)):³⁵

$$CE = \Delta OD / (Q/A) \quad (3)$$

$$\Delta OD = \log(T_b/T_c) \quad (4)$$

where Q is the integration of the current within the coloured time and A is the given electrode area. In general, a high value of the CE suggests that the EC materials show a large transmittance modulation with a small intercalation charge density. Fig. 4d shows the curve of OD at a wavelength of 633 nm as a function of intercalation charge density under a potential of -0.7 V. From the slope of line fitting the linear region of the curve, the calculated CE values are $34.5 \text{ cm}^2 \text{ C}^{-1}$ for bare WO_3 , $42.2 \text{ cm}^2 \text{ C}^{-1}$ for $\text{WO}_3/\text{C}5$, $51.4 \text{ cm}^2 \text{ C}^{-1}$ for $\text{WO}_3/\text{C}10$, and $32.1 \text{ cm}^2 \text{ C}^{-1}$ for $\text{WO}_3/\text{C}15$, indicating that the CE value enhances with an increase of the weight ratio of camphene and then decreases when the weight ratio of camphene reaches 15 wt%. As a result, $\text{WO}_3/\text{C}10$ exhibits a relatively high CE value as compared to the other samples in this study, thus providing a large transmittance modulation with a small applied charge density. This performance can be attributed to the combined effects of the mesoporous morphology and the increased oxygen vacancy defects in WO_3 . Based on these results, we propose the exceptional EC properties, including fast switching speeds and high CE of $\text{WO}_3/\text{C}10$ formed using the camphene-assisted sol-gel method, which can be defined as follows: the outstanding fast switching speeds (5.8 s for coloration speed and 1.0 s for bleaching speed) correlates with the combined effect of the mesoporous morphology reducing the Li^+ diffusion pathway and the increased oxygen vacancy defects providing the enhanced electrical conductivity. The enhanced CE ($51.4 \text{ cm}^2 \text{ C}^{-1}$) is due to a more effective electrostatic contact by the mesoporous morphology and the increased optical bandgap by the increased oxygen vacancy defects of the WO_3 , leading to a large transmittance modulation ($\Delta T = 73.3\%$) with respect to a small intercalation charge density.

Conclusions

In this study, we successfully fabricated unique mesoporous WO_3 films with oxygen vacancy defects using the camphene-assisted sol-gel method. Interestingly, our results demonstrate that camphene used as an organic additive has attractive multi-functions forming both mesopores and oxygen vacancy defects on the WO_3 films. By optimizing the weight ratio of camphene, the mesoporous WO_3 films with oxygen vacancy defects ($\text{WO}_3/\text{C}10$) prepared using 10 wt% camphene exhibit extraordinary EC properties with both fast switching speed

(5.8 s for coloration speed and 1.0 s for bleaching speed) and high CE ($51.4 \text{ cm}^2 \text{ C}^{-1}$). These outstanding EC properties can be defined by the combined effect of the mesoporous morphology and oxygen vacancy defects; the outstanding fast switching speeds are attributed to the reduced Li^+ diffusion pathway by the mesoporous morphology and the increased electrical conductivity by the oxygen vacancy defects. The improved CE value can be ascribed to the large transmittance modulation induced by both a more effective electrostatic contact with the electrolyte of the mesoporous morphology and the increased optical bandgap of the oxygen vacancy defects. Therefore, we propose that the mesoporous WO_3 films with oxygen vacancy defects formed using the camphene-assisted sol-gel method have high potential as a promising EC material for high-performance EC devices.

Conflicts of interest

There are no conflicts to declare.

Notes and references

- M. Layani, P. Darmawan, W. L. Foo, L. Liu, A. Kamyshny, D. Mandler, S. Magdassi and P. S. Lee, *Nanoscale*, 2014, **6**, 4572.
- H. Li, G. Shi, H. Wang, Q. Zhang and Y. Li, *J. Mater. Chem. A*, 2014, **2**, 11305.
- G. Gai, P. Darmawan, M. Cui, J. Chen, X. Wang, A. L.-S. Eh, S. Magdassi and P. S. Lee, *Nanoscale*, 2016, **8**, 348.
- G. Gai, J. Wang and P. S. Lee, *Acc. Chem. Res.*, 2016, **49**, 1469.
- J. Zhou, Y. Wei, G. Luo, J. Zheng and C. Xu, *J. Mater. Chem. C*, 2016, **4**, 1613.
- O. Arutanti, A. B. D. Nandiyanto, T. Ogi, T. O. Kim and K. Okuyama, *ACS Appl. Mater. Interfaces*, 2016, **15**, 3009.
- Y. Li, D. Chen and R. A. Caruso, *J. Mater. Chem. C*, 2016, **4**, 10500.
- S. K. Deb, *Sol. Energy Mater. Sol. Cells*, 2008, **92**, 245.
- F. Zheng, W. Man, M. Guo, M. Zhang and Q. Zhen, *CrystEngComm*, 2015, **17**, 5440.
- L. Yang, D. Ge, J. Zhao, Y. Ding, X. Kong and Y. Li, *Sol. Energy Mater. Sol. Cells*, 2012, **100**, 251.
- J. Z. Ou, S. Balendhran, M. R. Field, D. G. McCulloch, A. S. Zoolfakar, R. A. Rani, S. Zhuiykov, A. P. O'Mullane and K. Kalantar-zadeh, *Nanoscale*, 2012, **4**, 5980.
- S. R. Bathe and P. S. Patil, *Sol. Energy Mater. Sol. Cells*, 2007, **91**, 1097.
- X. Yang, G. Zhu, S. Wang, R. Zhang, L. Lin, W. Wu and Z. L. Wang, *Energy Environ. Sci.*, 2012, **5**, 9462.
- S. K. Deb, *Sol. Energy Mater. Sol. Cells*, 2008, **92**, 245.
- C.-P. Li, C. A. Wolden, A. C. Dillon and R. C. Tenent, *Sol. Energy Mater. Sol. Cells*, 2012, **99**, 50.
- S. R. Bathe and P. S. Patil, *Solid State Ionics*, 2008, **179**, 314.

- 17 Z. Jiao, M. Wu, Z. Qin and H. Xu, *Nanotechnology*, 2003, **14**, 458.
- 18 P. Porkodi, V. Yegnaraman and D. Jeyakumar, *Mater. Res. Bull.*, 2006, **41**, 1476.
- 19 M. Caiado, A. Machado, R. N. Santos, I. Matos, I. M. Fonseca, A. M. Ramos, J. Vital, A. A. Valente and J. E. Castanheiro, *Appl. Catal., A*, 2013, **451**, 36.
- 20 X. He, R. Xu, L. Zhang, F. Zhang, Z. Zhou and Z. Zhang, *Chem. Eng. Res. Des.*, 2016, **114**, 60.
- 21 K. N. Tu and U. Gösele, *Appl. Phys. Lett.*, 2005, **86**, 093111.
- 22 B.-R. Koo, S.-T. Oh and H.-J. Ahn, *Mater. Lett.*, 2016, **178**, 288.
- 23 J.-W. Bae, B.-R. Koo, H.-R. An and H.-J. Ahn, *Ceram. Int.*, 2015, **41**, 14668.
- 24 M. A. Habib and D. Glueck, *Sol. Energy Mater.*, 1989, **18**, 127.
- 25 C. Guo, S. Yin, Q. Dong and T. Sato, *CrystEngComm*, 2012, **14**, 7727.
- 26 Z. Gu, Y. Ma, T. Zhai, B. Gao, W. Yang and J. Yao, *Chem. - Eur. J.*, 2006, **12**, 7717.
- 27 Y. Zheng, G. Chen, Y. Yu, Y. Zhou and F. He, *Appl. Surf. Sci.*, 2016, **362**, 182.
- 28 A. P. Shpak, A. M. Korduban, M. M. Medvedskij and V. O. Kandyba, *J. Electron Spectrosc. Relat. Phenom.*, 2007, **156**, 172.
- 29 B. V. L'vov, A. A. Vasilevich, A. O. Dyakov and J. W. H. Lam, *J. Anal. At. Spectrom.*, 1999, **14**, 1019.
- 30 Y. A. Yang, Y. W. Cao, B. H. Loo and J. N. Yao, *J. Phys. Chem. B*, 1998, **102**, 9392.
- 31 L. Xiao, Y. Lv, W. Dong, N. Zhang and X. Liu, *ACS Appl. Mater. Interfaces*, 2016, **8**, 27107.
- 32 V. Etacheri, R. Roshan and V. Kumar, *ACS Appl. Mater. Interfaces*, 2012, **4**, 2717.
- 33 B. E. Sernelius, K.-F. Berggren, Z.-C. Jin, I. Hamberg and C. G. Granqvist, *Phys. Rev. B: Condens. Matter*, 1988, **37**, 10244.
- 34 E. Finazzi, C. D. Valentin and G. Pacchioni, *J. Phys. Chem. C*, 2009, **113**, 220.
- 35 D. Ma, H. Wang, Q. Zhang and Y. Li, *J. Mater. Chem.*, 2012, **22**, 16633.
- 36 R. Xu and Y. Xu, *Modern Inorganic Synthetic Chemistry*, Elsevier, Netherlands, 2017.
- 37 X. Ding, D. Zeng, S. Zhang and C. Xie, *Sens. Actuators, B*, 2011, **155**, 86.
- 38 C.-P. Li, F. Lin, R. M. Richards, C. Engtrakul, A. C. Dillon, R. C. Tenent and C. A. Wolden, *Electrochem. Commun.*, 2012, **25**, 62.
- 39 C.-P. Li, F. Lin, R. M. Richards, C. Engtrakul, R. C. Tenent and C. A. Wolden, *Sol. Energy Mater. Sol. Cells*, 2014, **121**, 163.
- 40 F. Lin, J. Cheng, C. Engtrakul, A. C. Dillon, D. Nordlund, R. G. Moore, T.-C. Weng, S. K. R. Williams and R. M. Richards, *J. Mater. Chem.*, 2012, **22**, 16817.
- 41 C. F. Cai, J. P. Tu, D. Zhou, X. L. Wang and C. D. Gu, *Sol. Energy Mater. Sol. Cells*, 2014, **124**, 103.
- 42 R. Yu, Z.-H. Meng, M.-D. Ye, Y.-H. Lin, N.-B. Lin, X.-Y. Liu, W.-D. Yu and X.-Y. Liu, *CrystEngComm*, 2015, **17**, 6583.
- 43 J. Denayer, P. Aubry, G. Bister, G. Spronck, P. Colson, B. Vertruyen, V. Lardot, F. Cambier, C. Henrist and R. Cloots, *Sol. Energy Mater. Sol. Cells*, 2014, **130**, 623.
- 44 T. Brezesinski, D. F. Rohlfiing, S. Sallard, M. Antonietti and B. M. Smarsly, *Small*, 2006, **2**, 1203.
- 45 L. Liu, M. Layani, S. Yellinek, A. Kamyshny, H. Ling, P. S. Lee, S. Magdassi and D. Mandler, *J. Mater. Chem. A*, 2014, **2**, 16224.